Synthesis of cobalt grown from Co-S eutectic in high magnetic fields

Steven Flynn,[1,*] Caeli L. Benyacko,[1,†] Matúš Mihalik,[2,‡] Jared Lee,[1,§] Fuyan Ma,[3] Michael E. Bates,[1,‖] Shubham Sinha,[1,¶] Khalil A. Abboud,[3] Marian Mihalik,[2] Mark W. Meisel,[1,4,5,#] and James J. Hamlin[1,**]

[1]*Department of Physics, University of Florida, Gainesville, Florida 32611-8440, USA*

[2]*Institute of Experimental Physics, Slovak Academy of Sciences, Watsonova 47, Košice 040 01, Slovakia*

[3]*Department of Chemistry, University of Florida, Gainesville, Florida 32611-7200, USA*

[4]*National High Magnetic Field Laboratory, University of Florida, Gainesville, Florida 32611-8440, USA*

[5]*Institute of Physics, Faculty of Science, P. J. Šafárik University, Park Angelinum 9, 040 01 Košice, Slovakia*

(Received 1 April 2025; accepted 1 August 2025; published 2 September 2025)

Samples of Co were grown directly in the ferromagnetic state under equilibrium conditions using a cobalt sulfide flux. Magnetic fields up to 9 T were applied during growth, and isolated Co products exhibit progressively elongated morphologies, from cubes to rectangular rods to needlelike tendrils with poorly defined facets. The degree of elongation of the major axis was found to correlate with magnetic field direction, strength, and gradient. Two-dimensional x-ray diffraction data indicate some level of polycrystallinelike samples, and quantitative analyses (Le Bail and Rietveld) of the one-dimensional data confirm the presence of hcp and fcc phases. The magnetic responses indicate a partial alignment of the magnetic easy axis of the hcp phase along the magnetic field present during growth.

DOI: 10.1103/9bb3-4pby

I. INTRODUCTION

With goals of accessing new phases and/or improving physical properties of products, the application of high magnetic fields during materials synthesis and processing at high temperatures has been the subject of research for at least four decades [1–8]. An initial impression is that the presence of the magnetic field is not expected to have a significant effect because the ratio of the magnetic to thermal energy is estimated to be small, e.g., $\mu_{\text{eff}}B/k_{\text{B}}T \lesssim 0.1$ for $\mu_{\text{eff}} = 5\,\mu_{\text{B}}$, $B = 10\,\text{T}$, and $T = 300\,\text{K}$, where k_{B} is the Boltzmann constant and μ_{B} is the Bohr magneton. Contrarily, an increasing number of materials have been reported to possess altered properties when being synthesized or processed at extreme magnetothermal conditions [9–14].

The present work addresses the specific endeavor to grow and characterize single crystalline Co grown at temperatures below the Curie temperature of the solid by using a cobalt-sulfide flux, as suggested by Canfield and coworkers in 2012 [15–17], Fig. 1. Possessing the highest known Curie temperature ($T_{\text{C}} = 1121\,^{\circ}\text{C} = 1394\,\text{K}$) of any single element, cobalt is an ideal model whose structural and magnetic properties are well studied [18–25]. In fact dating back to the early 2000s, Beaugnon and collaborators have generated Co products from Co-B [26–33], Co-Cu [34–37], and Co-Sn [38–42] melts. More specifically, working with supercooled melts, solidification of the product directly in the ferromagnetic phase was achieved despite the melting point being higher than the T_{C}. Although the transition from a mobile liquid metal phase solidifying into a ferromagnetic state enhances the development of magnetic field effects, the nonequilibrium precipitation from a supercooled melt effects the crystallization process, thereby perturbing the crystal structure, microstructure, morphology, and properties of the products. Herein, Co samples were directly crystallized in the ferromagnetic state under equilibrium conditions using a low melting Co-S eutectic.

After describing the methods and experimental arrangements, the macroscopic and microscopic structural analyses, along with magnetic and conductivity properties, are presented and discussed. Lastly, this work and its findings are summarized to indicate future extensions that are beyond the scope of this initial attempt. For example, the well-defined facets observed in our products provide an example of potential properties that may be uniquely accessed by an equilibrium precipitation in high magnetic fields.

II. EXPERIMENTAL DETAILS

A. Furnace magnet

A custom insert was designed and built so a 1200 °C resistive furnace could be operated in an 89 mm, room-temperature

*Present address: Department of Chemistry, Johns Hopkins University, Baltimore, Maryland 21218, USA.

†Present address: Materials Department, University of California, Santa Barbara, California 93106-5050, USA.

‡Deceased, 23 April 2025.

§Present address: Department of Physics, Syracuse University, Syracuse, New York 13244, USA.

‖Present address: Sandia National Laboratories, Albuquerque, New Mexico 87185, USA.

¶Present address: Carnegie Institute for Science, Washington, DC 20015, USA.

#Contact author: meisel@ufl.edu

**Contact author: jhamlin@ufl.edu

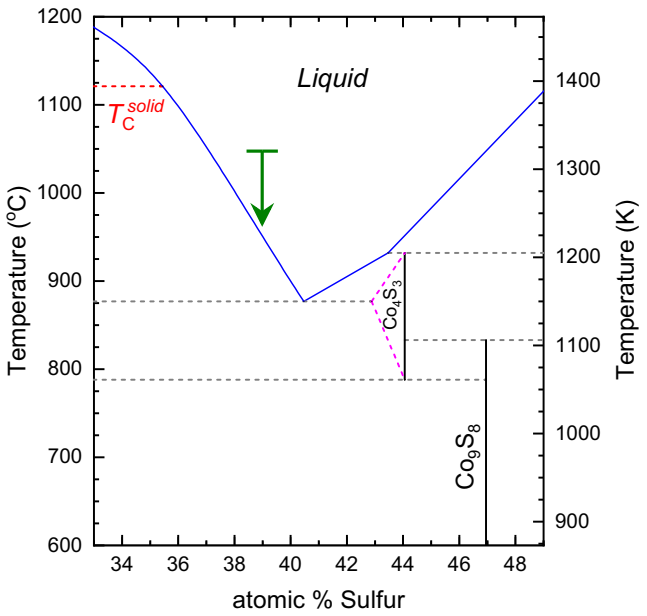

FIG. 1. The Co-S binary alloy phase diagram, adapted from [18] which is reproduced and given in [19], presumably based on aspects of another compilation [20], is shown in the region of interest for this work.[1] The liquidus boundary is shown in blue, and the Curie temperature for pure solid cobalt is shown in red. The expected path of our composition $Co_{61}S_{39}$ is shown by the green arrow, whose base is located at the hold temperature of 1050 °C and body spans the slow-cooling path to nominally 950 °C, where crystallization occurs as the liquidus line is encountered.

[1]It is important to note this phase diagram was generated in the absence of an applied magnetic field.

bore of an Oxford Instruments 9.4 T NMR superconducting magnet, whose current was adjusted to provide a specific field value and then set in persistent mode for fixed field operation. The unit, whose details are described in the Appendix, consists of the integration of three main components, namely a water-cooled, heat-exchanging outer jacket, an interior resistive heater unit, and extra passive insulation and support.

B. Synthesis and isolation of Co products

Cobalt samples were synthesized using a Co-S binary flux [15–17]. Stoichiometric amounts of Co (Cerac, 99.5%) and S (Alfa Aesar, 99.9995%) were precisely weighed to give a final composition of $Co_{61}S_{39}$. This ratio was selected to target the Co-rich side of the Co-S eutectic while fixing the liquidus temperature below 1050 °C as a practical consideration, Fig. 1. Sample mixtures were placed in an alumina crucible with the low melting S on top, and the loaded reaction vessel was subsequently sealed in a quartz tube after five cycles of evacuation and flushing with Ar gas. The sealed tubes were subsequently loaded into a custom-designed furnace situated in the room-temperature bore of the superconducting magnet. Samples were heated at a rate of 5 °C/min to 1050 °C, held for 24 hours, cooled at a rate of 1 °C/hr to 900 °C, and then cooled to room temperature while remaining in the furnace. This process was performed while the field of the magnet was held constant at either $B = 0$, 3, or 9 T. It is important to note, the furnace-magnet system does not presently allow the sample to be rapidly removed for centrifuging to remove flux due to the large magnetic forces present in the field gradient region.

TABLE I. Product nomenclature, magnetic field and gradient during synthesis, saturation magnetization M_{sat}, room-temperature resistivity, and RRR [$= \rho(300\,K)/\rho(5\,K)$] values.

Name	B (T)	∇B (T/cm)	M_{sat} (μ_B/atom)	$\rho(300\,K)$ μΩ cm	RRR
0 T	0	$<10^{-3}$	1.66	11.0	2.4
3 T	3	$<10^{-3}$	1.72	5.6	14.6
9 T	9	$<10^{-3}$	1.60	5.6	2.6
9 T+∇	8.8 ± 0.1	0.2 ± 0.1	1.61	8.8	4.7

In a fixed field, several synthesis runs were performed in the center of the homogeneous field region, where the field variation was less than 0.1% over the synthesis region, and Co pieces extracted from the Co-S boule were labeled by the synthesis field. In one instance, the synthesis occurred 6.35 ± 0.51 cm below the center of the homogeneous field region, where the field and its gradient were approximately 8.8 ± 0.1 T and 0.10 ± 0.05 T/cm. The resultant Co products are described in Table I.

As shown in in Fig. 2, reacted samples typically consisted of a boule of solidified flux surrounding the Co flux products. The latter were mechanically separated from the former through careful application of force to the relatively brittle flux matrix. Flux products were identified visually through their distinct, metallic appearance and clear facets in some cases. Pieces from the Co regions were extracted in sizes and orientations appropriate for the subsequent characterization technique.

C. Characterization

The x-ray data were collected on a Bruker Dual microsource D8 Venture diffractometer and PHOTON III detector running the APEX3 software package of programs and using Mo K_α radiation (0.71073 Å). Phi scans with a sweeping angle of 0.1° were performed on the sample at different 2Θ angles to get Debye rings. The obtained Debye rings were integrated in APEX3 and converted into one-dimensional patterns. Additional analysis was performed using FullProf software [43] for Le Bail [44] and Rietveld [45] analysis.

Magnetic data were collected on a Quantum Designs MPMS XL SQUID Magnetometer with a magnetic range of ±7 T and a thermal range of 2 K to 300 K. The typical characterization sequence involved initial zero-field cooling (ZFC) to 5 K, measuring the temperature dependence of magnetization in 10 mT from 5 K to 300 K, and then measuring while field cooling (FC) to 5 K. Isothermal magnetization studies were performed by fixing the temperature and then sweeping the magnetic field from a low value to 7 T and then reducing the field while measuring to −1 T. Samples

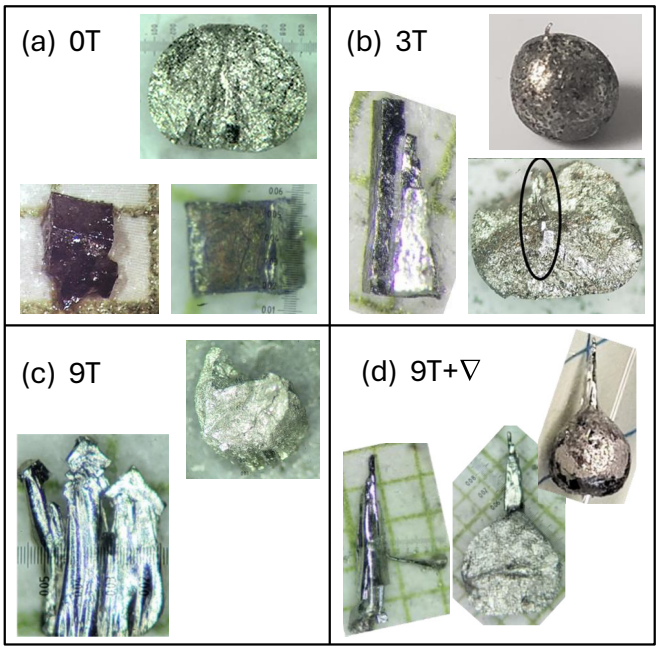

FIG. 2. Photographs of samples described in Table I. (a) 0 T: a cross-sectional view of about half the boule after first application of gentle force, where the characteristic flattened bottom is seen, and the small dark region is the Co crystal shown in the other two views after boule residue has been carefully removed; (b) 3 T: the boule as grown, sitting on its bottom, with tip at the top noticeable, then a view looking down on the remaining boule after some processing to extract the Co piece, which is from the tip region circled in black, and shown as fully extracted; (c) 9 T: a view of the boule, resting on its flattened bottom after some processing and the region, where the Co piece was extracted, is visible on the side near the bottom of the image, and the extracted Co piece is shown; and (d) $9\,\mathrm{T} + \nabla$: a side view of the boule as grown notably without a flatten bottom so it is laying on its side, followed by an image after some processing has been performed, and a view of the Co dendrite that was extracted for characterization, shown with a piece to the side due to the exceedingly soft nature of the resulting structure. The background green paper grid, if present, provides a scale of 1 mm, while in some micrographs an arbitrary scale bar from the lens is visible.

were mounted in No. 5 gelatin capsules and variable amounts of eicosane were used to preserve orientation. The magnetic contributions of both the capsule and eicosane were found to be less than the uncertainty of the total magnetic signal and were therefore considered negligible. Demagnetizing effects were also considered in respect to the geometry of the sample. Specific demagnetizing factors were calculated using the formula outlined by Bahl [46] assuming a rectangular prism geometry. The overall shift due to demagnetization was minimal.

Resistivity data were collected with a Quantum Design PPMS using a Keithley 6221/2182A arrangement operating in delta mode over a range of 5 K–300 K at a rate of 5 K/min. Four wires were attached to samples with silver paint in the van der Pauw configuration for the 0 T sample, and in a linear configuration for other samples as long, thin pieces were isolated from the products.

III. RESULTS AND DISCUSSION

A. Macroscopic shapes/properties

The main piece of the zero-field control, referred to as 0 T, appears to be a rectangular prism exhibiting multiple perpendicular, well-defined facets and sharp edges, Fig. 2(a). Notably, the sample morphology resembles a pseudo tetragonal habit with side-lengths within 10% of each other and the third, shorter side ending in a jagged, poorly-defined face, suggesting an interrupted crystallization process in that direction. The overall appearance is consistent with the long-standing conception of Co adopting a fcc structure at high temperature and suggests our heating profile successfully produced single crystals during their initial formation [21–25].

Obtaining the fcc phase at low temperature typically requires a rapid quench of the sample. However, our apparatus does not currently permit the rapid removal of the sample required to accomplish a full quench of the fcc phase. Instead, the sample is cooled gradually through the fcc → hcp transition temperature. Consequently, the elongated single crystals of fcc Co formed in high field largely transition to the hcp structure during cooling, and this process is reported to split crystals [23,25,47]. In other words, the initial single crystals of fcc Co are broken into a polycrystalline sample involving a mixture of fcc and hcp structures. Due to the complex inhomogeneous strains that develop during the transition, the resulting smaller crystalline domains may not maintain perfect orientation along the field direction. This general description is supported by the results and interpretations of others groups [2,48], including Bu *et al.* in their work with the undercooled Co-B eutectic alloy in strong magnetic fields [33].

Recently Sewak, Dey, and Toprek [50] have reported the hcp phase is stabilized at both low and high temperatures (∼600 °C) whereas the fcc phase is stabilized near 227 °C, although the hcp phase was found to be the dominant low temperature phase. Ultimately, as will be discussed, all of the products reported herein possess a polycrystallinelike nature. Herein, we use the term "polycrystallinelike" because the products possess a mix of hcp and fcc domains which have preferred orientation along the magnetic field.

For the 3 T sample, Fig. 2(b), clear facets and mutually perpendicular faces are evident in the flux products. However, the longest dimension has become distinct from the others by at least an order of magnitude, giving the product the appearance of an extended, rigid rod rather than a cube or box. This pattern is further evolved for the 9 T sample, Fig. 2(c), where a mass of smooth, nonfaceted columns of indeterminate morphology are capped with small, faceted rectangular prisms.

Lastly, the morphology of the $9\,\mathrm{T} + \nabla$ sample, Fig. 2(d), possess additional different aspects as little to no faceting is present along a smoothly tapered dendrite that is more elongated relative to its thickness than the rods observed in the 3 T sample, Fig. 2(a). Initially the dendrite was straight, like a needle, and embedded in a cluster much like the 9 T product, Fig. 2(c). However, further processing revealed a cluster/bundle terminated in faceted feet. Carefully using tweezers, light pulling revealed the dendrite was exceptionally flexible, as expected for a pure, annealed metal [51–53], but

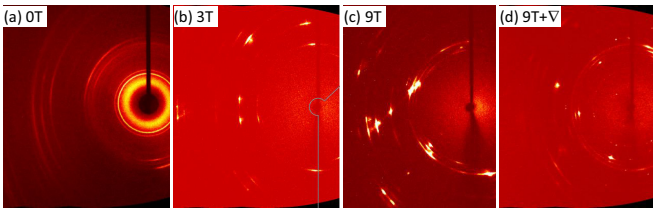

FIG. 3. Merged two-dimensional diffraction patterns collected on the samples listed in Table I. The Debye rings possess polycrystallinelike features, with randomly oriented grains in the 0 T sample. The samples grown in finite fields show clear evidence of significant texture.

could be pulled out of the cluster, Fig. 2(d), although some plastic deformation resulted.

Overall, the elongation is likely a result of a combination of effects, one of which includes the magnetocrystalline anisotropy of Co [54]. More specifically, the magnetic easy axis of fcc Co is the [111] direction [25], and this magnetic anisotropy produces a small reduction in the Zeeman energy for Co crystals with their [111] axes aligned with the applied field compared to those with a different orientation. Although this energy difference is small, as the anisotropy constants for fcc cobalt at 950 °C are of order 10^{-6}, this variation has a sizable influence on nucleation rates, which are exponential in the free energy difference between the liquid and solid phase. Thus, the nucleation rate for solid fcc Co with the [111] axis aligned with the field will be enhanced, and upon cooling through the fcc → hcp transition, the hcp crystals are partially aligned with their easy axis along the magnetic field present during growth, as evidenced by the magnetic data, *infra vide*.

B. XRD data and interpretations

Merged two-dimensional diffraction patterns collected for the samples are shown in Fig. 3. The Debye rings show some evidence of polycrystallinity, with randomly oriented grains in the 0 T sample. For synthesis in finite magnetic fields, the samples show a mix of rings and spots indicative of significant texture.

The results of the conversion of the data to total intensity versus 2θ plots are shown in Fig. 4. Several peaks with exceptionally large intensities and low peak widths (FWHM $<0.05°$) have been omitted for clarity and are attributed to artifacts of the merging and integration process, thereby resulting in some small breaks in the data curves. The results of the Le Bail analysis are also shown, where a mixture of contributions from hcp and fcc phases of cobalt, along with monoclinic sulfur, provide suitable and plausible fits using the parameters given in Table II.

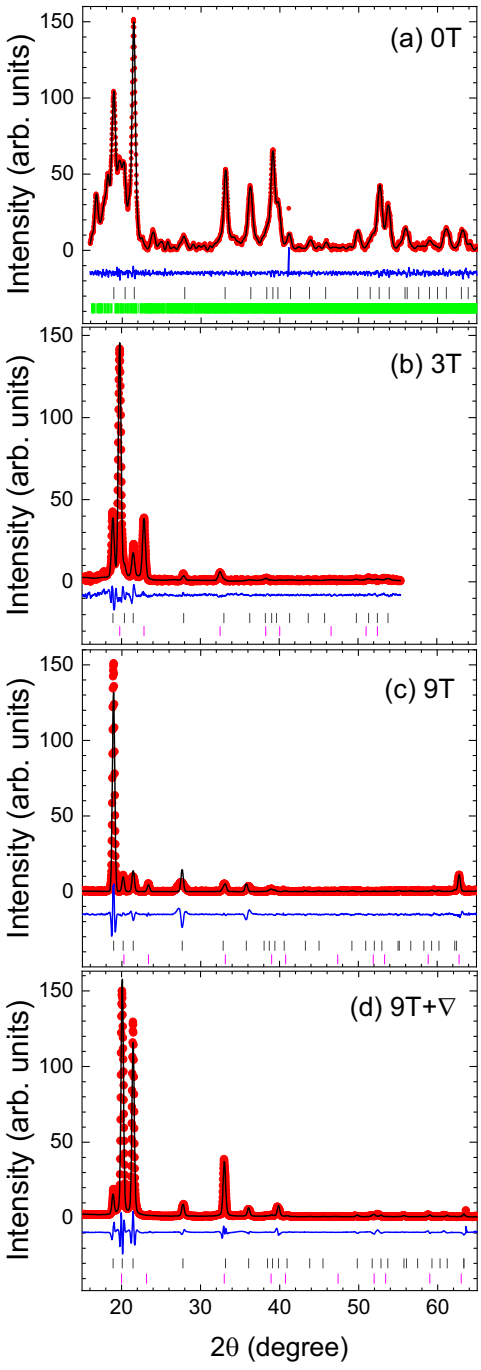

FIG. 4. The Le Bail fits of the integrated data from Fig. 3. Dots are the integrated data, and the black line is the best Le Bail fit. Below the data, the blue line is the difference, and the ticks represent Co hcp (dark gray), Co fcc (magenta), and monoclinic S (green). The refined lattice parameters are reported in Table II.

TABLE II. Lattice parameters used in the analysis of the XRD data, as contrasted to reference values.

	Hexagonal		Cubic	
Name	a (Å)	c (Å)	a (Å)	Ref.
Co hcp	2.5071	4.0686		[55]
Co fcc			3.55 (3.54)	[56] ([55])
0 T	2.504	4.031		S [57]
3 T	2.510	4.036	3.601	
9 T	2.541	4.133	3.563	
9 T+∇	2.486	4.057	3.530	

Not surprisingly, the 0 T control sample, which was encased in (and extracted from) surrounding flux, Fig. 2(a), possesses Co hcp with a significant amount of other contri-

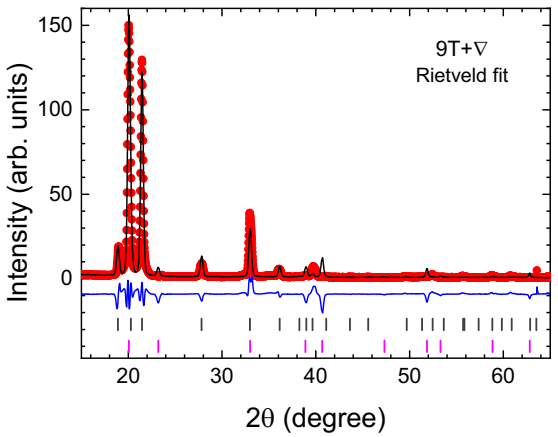

FIG. 5. The Reitveld fitting results for the 9 T + ∇ data also used in Fig. 4(d). Dots are the integrated data, and the black line is the best Reitveld fit. Below the data, the blue line is the difference, and the ticks represent Co hcp (dark gray) and Co fcc (magenta).

butions, which are modeled as monoclinic S, Fig. 4(a). The other contributions are likely poorly crystalline or amorphous phases of Co_xS_y and S flux. For the synthesis in the presence of a magnetic field, the isolated products, which were partially or fully emerged from the flux, Figs. 2(b)–2(d), are generally comprised of a mix of hcp and fcc Co phases. Quantitative comparisons of these results with values reported in the literature are provided in Table II, where the outcomes from the Le Bail fitting are within 1–2% of the published values for hcp Co and are reasonably close to the ones for fcc Co. While the space group fits both structures, the obvious issue is the study was not performed on powder or single crystals, nevertheless the lattice parameters were resolved. In addition, the samples are not simply polycrystalline, so the estimate of the ratio between the two phases was not possible.

In an attempt to further quantify the XRD data, Rietveld analysis was attempted for the three samples synthesized in a magnetic field, Figs. 4(b)–4(d). Even with generous standards, the outcomes for the 3 T and 9 T samples did not converge to physically plausible results. On the other hand, although not suitable for standard powder analysis, the Rietveld results for the 9 T + ∇ sample, Fig. 5, are reasonably the same as the outcome of the Le Bail fit, Fig. 4(d), with identical lattice parameters provided by both fitting schemes, Table II.

C. Magnetic properties

The temperature and magnetic field dependences of the magnetic responses of the samples reported herein are shown in Fig. 6. The temperature dependence of the magnetization is similar for all samples except for the 9 T + ∇ response. The isothermal magnetic field dependence of the magnetization suggests the 3 T and 9 T + ∇ samples possess partial alignment of the magnetic easy axis ([0001] or *c* axis) of their hcp phases along the field direction present during the synthesis process, see Fig. 6(b).

For the samples reported herein, saturation magnetization was achieved nominally about 3 T, independent of orientation of the sample, and the resulting magnetic moments are reported in Table I. The M_{sat} values for all samples

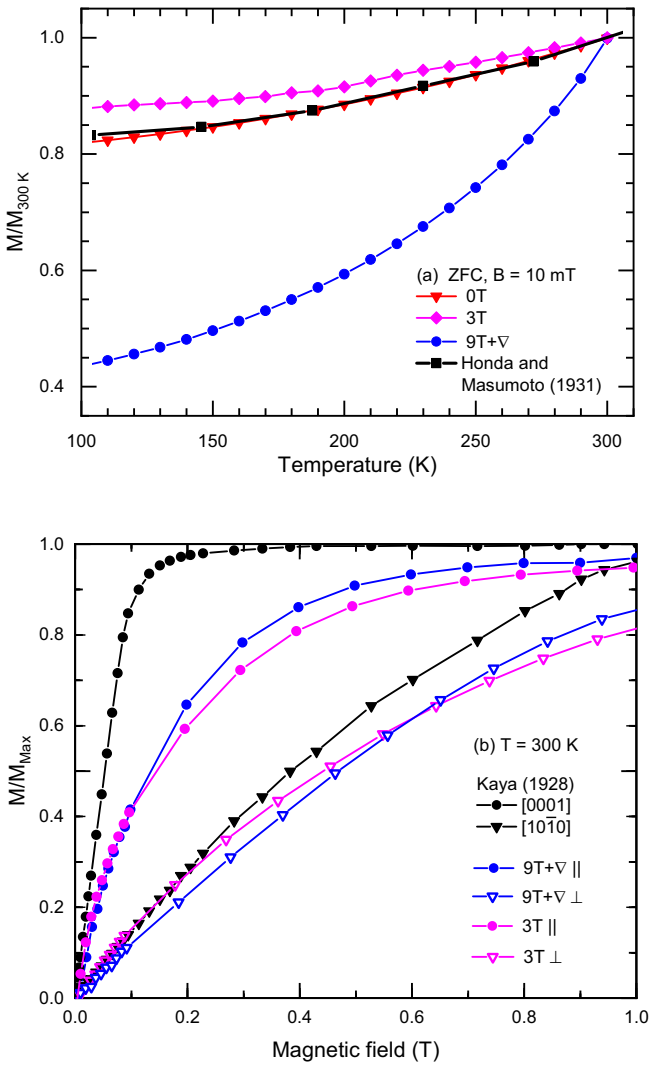

FIG. 6. The temperature and magnetic field dependences of the magnetic responses are shown. (a) The temperature dependences of the zero-field cooled (ZFC) responses of the magnetization, M, normalized to the value at 300 K, $M_{300\,K}$, and measured while warming from 5 K, are shown over the temperature region that overlaps the data reported by Honda and Masumoto [21]. (b) The isothermal (T = 300 K) magnetization, M, responses, normalized to the maximumum value observed/reported, M_{max}, are shown over the field region that overlaps the data reported for a single-crystal of Co studied by Kaya [22]. Parallel (||) and perpendicular (⊥) symbols refer to the direction of the measuring magnetic field compared to the growth direction along the field present during synthesis.

are in the range of $1.60 - 1.72\ \mu_B$ per atom, assuming the sample is pure cobalt. These values can be contrasted with others reported in experimental studies [58–61] and theoretical/numerical works [62–65].

D. Conductivity measurements

For an additional perspective on properties of the products, the resistivity as a function of temperature for several samples was measured, and in every instance, the data exhibited behavior typical for a simple metal, namely a near-linear tem-

perature dependence from room temperature that smoothly transitions to a temperature-independent region starting below nominally 30 K. At room temperature, pure Co is reported to have a resistivity in the range of $5.2 - 5.9\ \mu\Omega$ cm [66], and although the values observed for the 9 T and 3 T samples are in this range, larger ones were obtained for the 0 T and $9\,\mathrm{T} + \nabla$ samples. In addition, relatively low residual resistivity ratios [54], RRR $= \rho(300\,\mathrm{K})/\rho(5\,\mathrm{K})$, were observed for all samples, but pure Co is notoriously known to possess rather low RRR values, typically reaching only $20 - 60$ [66]. The resistivity results are summarized in Table I. Bloch-Gruneisen fits [67] to the electrical resistivity data (not shown but available [68]) give values of the Debye temperature of 480 ± 30 K, which is consistent with 460 K, which is the reported value for cobalt in the low temperature limit [69].

Together, these data provide little definitive insight into the specific nature of the samples produced and investigated. Nevertheless, benchmarks for future work are established, while also providing an important caveat to avoid cold working the samples after production.

IV. SUMMARY

Using an unusual combination of a furnace operating inside the room-temperature bore of a superconducting magnet, a striking suggestion to explore equilibrium materials synthesis in an exotic combination of parameter space was realized. Specifically, samples of Co were grown directly in the ferromagnetic state under equilibrium conditions using a cobalt sulfide flux, as suggested by Canfield and coworkers some years ago [15–17]. Indeed, in equilibrium conditions while in the presence of magnetic fields up to 9 T, Co products were found to exhibit progressively elongated morphologies that were enhanced in the presence of a gradient field. The findings reported herein provide a preliminary step to designing explicit refinements required for the Co-S studies, while also facilitating the nucleation of other investigations targeting new and metastable phases of materials that are not accessible with present protocols and techniques.

ACKNOWLEDGMENTS

The authors acknowledge enlightening conversations with Ryan Baumbach, Paul Canfield, Bill Malphurs, Theo Sigrist, and Kaya Wei. This work and the development of the high-field furnace insert and related instrumentation was supported by the U.S. Department of Energy's Office of Energy Efficiency and Renewable Energy (EERE) under the Industrial Efficiency & Decarbonization Office (IEDO) Award No. DE-EE0009131. The views expressed herein do not necessarily represent the views of the U.S. Department of Energy of the United States Government or any agency thereof. The 9.4 T magnet and the associated facility were supported by the National High Magnetic Field Laboratory (NHMFL or MagLab) funded by the National Science Foundation (NSF) cooperative agreement DMR-1644779 and the State of Florida. Additional NSF support for the Research Experiences for Undergraduates (REU) was provided by DMR-1708410 (Spring 2022), DMR-1852138 (Summer 2022), MagLab DMR-1644779 (Fall 2022), and MagLab DMR-2128556 (Spring 2023, Fall 2023, and Spring 2024). Major aspects of this work were interrupted by the pandemic, and the impact of perturbations of evolving personnel changes led to a delay in the generation of this manuscript.

DATA AVAILABILITY

The data that support the findings of this article are openly available [68].

APPENDIX: DETAILS OF FURNACE

The cooling jacket is a double-walled cylinder constructed from two 316 stainless steel pipes selected as a nonmagnetic material with favorable mechanical properties to resist damage from heat and pressure. The overall outer and inner diameters of the jacket are 76.2 mm (3 in) and 63.5 mm (2.5 in), respectively, and both cylinders are 1.59 mm (1/16 in) thick. This arrangement leaves an empty 3.18 mm cylindrical shell within the jacket through which closed-cycle, chilled water at $15 - 20\,^{\circ}\mathrm{C}$ is passed at 4 ± 0.15 gpm. To ensure uniform cooling, a custom manifold splits the incoming water into eight 1.59 mm (1/16 in) I.D. turrets distributed uniformly around the bottom circumference of the jacket. The return chilled water exists a single 12.7 mm outlet at the top of the jacket. Pressure gauges, a flow meter, and type-K thermocouples monitor the condition of the chilled water at both the inlet manifold and the outlet port, thereby allowing for automatic shutdown if abnormal or dangerous conditions are detected.

The furnace consists of a ceramic fiber heater (Watlow, VC400J12A) with an inner diameter of 12.7 mm (0.5 in), an outer diameter of 50.8 mm (2 in), and a length of 304.8 mm (12 in). The nickel chromium heating elements are arranged in two counterwound solenoids embedded in ceramic fiber insulation. The furnace is positioned with its center 304.8 mm (12 in.) from the bottom of the cooling jacket, where the power leads exit. A hollow thermocouple port (I.D. 3.56 mm, 0.14 in) extends radially from the outer wall into the hollow core of the furnace halfway up its length. Protected with alumina insulation, a type-N thermocouple traverses the length of the furnace from the bottom of the jacket to this port. The type-N thermocouple was selected as a nonmagnetic alternative to type-K with a similar operational temperature range ($-270 - 1260\,^{\circ}\mathrm{C}$) [70]. The output is used by a programmable temperature controller (Watlow, F4SH-FAA0-01RG) to reach or maintain the desired heating rate and/or temperature. Current is supplied by a 150 V, 3.5 A DC power supply (Kepco) to avoid potential damage associated with the magnetic forces that would be exerted on the heating element wires with alternating current.

The furnace is wrapped in a layer of 6.35 mm (0.25 in) thick ceramic fiber blanket which helps keep it centered, limits heat losses at the outside wall, and provides friction which prevents its position from shifting vertically within the cooling jacket. A 152.4 mm (6 in) cylinder of fiberboard insulation is also positioned underneath the furnace as additional support. The inner diameter houses an alumina tube with I.D. 15.9 mm (5/8 in) that protects the insulation from abrasion when samples are inserted or removed. This assembly rests

on a cap fixed at the bottom of the cooling jacket leaving only the central bore open for access to the furnace chamber. Likewise, a column of ceramic fiber insulation with a central alumina tube sits on top of the furnace and fills the rest of the cooling jacket. During operation, thermal baffles made from thin, central alumina rods with fiberboard disks are inserted through the top and bottom alumina tubes to reduce heat loss.

The technical manual composed during the construction and operation of the UF Physics $B \times T$ instrument is available online [71].

[1] U. E. Steiner and T. Ulrich, Magnetic field effects in chemical kinetics and related phenomena, Chem. Rev. **89**, 51 (1989).

[2] P. de Rango, M. Lees, P. Lejay, A. Sulpice, R. Tournier, M. Ingold, P. Germi, and M. Pernet, Texturing of magnetic materials at high temperature by solidification in a magnetic field, Nature (London) **349**, 770 (1991).

[3] E. Beaugnon, D. Bourgault, D. Braithwaite, P. de Rango, R. Perrier de la Bathie, A. Sulpice, and R. Tournier, Material processing in high static magnetic field. a review of an experimental study on levitation, phase separation, convection and texturation, J. Phys. I France **3**, 399 (1993).

[4] C. Koch, Experimental evidence for magnetic or electric field effects on phase transformations, Mater. Sci. Eng., A **287**, 213 (2000).

[5] Edited by M. Yamaguchi and Y. Tanimoto, *Magneto-Science: Magnetic Field Effects on Materials: Fundamentals and Applications*, Springer Series in Materials Science (Springer, Berlin, Heidelberg, 2007).

[6] Z. Sun, M. Guo, J. Vleugels, O. Van der Biest, and B. Blanpain, Strong static magnetic field processing of metallic materials: A review, Curr. Opin. Solid State Mater. Sci. **16**, 254 (2012).

[7] G. Cao, H. Zhao, B. Hu, N. Pellatz, D. Reznik, P. Schlottmann, and I. Kimchi, Quest for quantum states via field-altering technology, npj Quantum Mater. **5**, 83 (2020).

[8] C. Wei, J. Wang, Y. He, J. Li, and E. Beaugnon, Solidification of immiscible alloys under high magnetic field: A review, Metals **11**, 525 (2021).

[9] R. Jaramillo, S. Babu, G. Ludtka, R. Kisner, J. Wilgen, G. Mackiewicz-Ludtka, D. Nicholson, S. Kelly, M. Murugananth, and H. Bhadeshia, Effect of 30T magnetic field on transformations in a novel bainitic steel, Scr. Mater. **52**, 461 (2005).

[10] K. Koyama, Y. Mitsui, E. S. Choi, Y. Ikehara, E. C. Palm, and K. Watanabe, Change of the equilibrium state of ferromagnetic mnbi by high magnetic fields, J. Alloys Compd. **509**, L78 (2011).

[11] D. E. Laughlin, Magnetic transformations and phase diagrams, Metall. Mater. Trans. A **50**, 2555 (2019).

[12] D. Weiss, B. Murphy, M. J. Thompson, H. B. Henderson, G. M. Rios, Orlando Ludtka, A. Perron, and M. S. Kesler, Thermomagnetic processing of aluminum alloys during heat treatment, Int. J. Metalcast. **15**, 49 (2021).

[13] K. Wang, C.-j. Yan, C.-h. Yuan, X.-c. Yang, L.-j. Zhao, and Q. Wang, Progress in research on diffusional phase transformations of fe–c alloys under high magnetic fields, J. Iron Steel Res. Int. **29**, 707 (2022).

[14] M. E. Hurley, R. K. Bollineni, A. M. Donald, S. Flynn, J. J. Hamlin, M. S. Kesler, M. V. Manuel, M. W. Meisel, L. Li, and V. M. Miller, Microstructural evolution of steel during magnetic field-assisted processing, JOM **77**, 2862 (2025).

[15] X. Lin, S. L. Bud'ko, and P. C. Canfield, Development of viable solutions for the synthesis of sulfur bearing single crystals, Philos. Mag. **92**, 2436 (2012).

[16] X. Lin, Development and exploration of potential routes of discovery of new superconductors, Ph.D. thesis, Iowa State University, Ames, 2013.

[17] P. C. Canfield, New materials physics, Rep. Prog. Phys. **83**, 016501 (2020).

[18] Edited by T. B. Massalski, H. Okamoto, P. R. Subramanian, and L. Kacprzak, *ASM Handbook: Alloy Phase Diagrams*, 2nd ed. (ASM International, Materials Park, OH, 1990), Vol. 3, Chap. Co(Cobalt) Binary Alloy Phase Diagrams, pp. 1232–1233.

[19] Edited by H. Okamoto, M. E. Schlesinger, and E. M. Mueller, *ASM Handbook: Alloy Phase Diagrams*, 3rd ed. (ASM International, Materials Park, OH, USA, 2016), Vol. 3, Chap. Co(Cobalt) Binary Alloy Phase Diagrams, p. 274.

[20] H. Rau, Range of homogeneity and defect energetics in Co1-xS, J. Phys. Chem. Solids **37**, 931 (1976).

[21] K. Honda and H. Masumoto, On the magnetization of single crystals of cobalt at high temperatures, Sci. Rep. Tohoku Imp. Univ. **20**, 323 (1931).

[22] S. Kaya, On the magnetisation of single crystals of cobalt, Sci. Rep. Tohoku Imp. Univ. **17**, 1157 (1928).

[23] Z. Nishiyama, X-ray investigation of the mechanism of the transformation from face centered cubic lattice to body centered cubic, Sci. Rep. Tohoku Imp. Univ. **23**, 637 (1934).

[24] H. Myers and W. Sucksmith, The spontaneous magnetization of colbalt, Proc. R. Soc. London A **207**, 427 (1951).

[25] W. Sucksmith and J. Thompson, The magnetic anisotropy of colbalt, Proc. R. Soc. London A **225**, 362 (1954).

[26] F. Gaucherand and E. Beaugnon, Magnetic texturing in ferromagnetic cobalt alloys, Phys. B: Condens. Matter **346-347**, 262 (2004).

[27] J. Wang, Y. He, J. Li, R. Hu, H. Kou, and E. Beaugnon, Overheating dependent undercooling in a hypoeutectic Co–B alloy, Mater. Chem. Phys. **149-150**, 17 (2015).

[28] Y. He, J. Li, J. Wang, and E. Beaugnon, Transition from hypereutectic to hypoeutectic for rapid solidification in an undercooled Co-B alloy, J. Cryst. Growth **499**, 98 (2018).

[29] Y. He, J. Li, J. Wang, E. Yildiz, S. Pairis, and E. Beaugnon, Temperature-induced structure transition in a liquid Co-B eutectic alloy, Mater. Lett. **234**, 351 (2019).

[30] Y. He, J. Li, L. Li, J. Wang, E. Yildiz, and E. Beaugnon, Composition dependent characteristic transition temperatures of Co-B melts, J. Non-Cryst. Solids **522**, 119583 (2019).

[31] Y. He, Y. Wu, F. Bu, C. Zou, Z. Bian, Q. Huang, T. Liu, Q. Wang, J. Wang, J. Li, and E. Beaugnon, Effects of an ultrahigh magnetic field up to 25 T on the phase transformations of undercooled co-b eutectic alloy, J. Mater. Sci. Technol. **93**, 79 (2021).

[32] Y. He, F. Bu, Y. Wu, J. Zhang, D. Luo, Z. Bian, Q. Zhou, T. Liu, Q. Wang, J. Wang, H. Wang, J. Li, and E. Beaugnon, Liquid state dependent solidification of a Co-B eutectic alloy under a high magnetic field, J. Mater. Sci. Technol. **116**, 58 (2022).

[33] F. Bu, Y. Zhang, H. Liu, J. Wang, E. Beaugnon, J. Li, and Y. He, Magnetic field intensity dependent microstructure evolution and recrystallization behavior in a co–b eutectic alloy, J. Mater. Sci. Technol. **138**, 93 (2023).

[34] J. Wang, J. Li, H. Kou, and E. Beaugnon, Instability pattern formation in a liquid metal under high magnetic fields, Sci. Rep. **7**, 2248 (2017).

[35] C. Wei, J. Wang, Y. He, Y. Yan, J. Gao, J. Li, and E. Beaugnon, Liquid-liquid phase separation in immiscible Cu-Co alloy, Mater. Lett. **268**, 127585 (2020).

[36] C. Wei, J. Wang, Y. He, Y. Yan, E. Beaugnon, and J. Li, Magnetic field induced instability pattern evolution in an immiscible alloy, Appl. Phys. Lett. **123**, 254101 (2023).

[37] C. Wei, J. Li, B. Dong, C. Huang, L. Wang, Y. Yan, Y. He, E. Beaugnon, and J. Wang, Tailoring the microstructure and properties of a Cu–Co immiscible alloy by high magnetic field assisted heat treatment, Mater. Chem. Phys. **302**, 127706 (2023).

[38] F. Gaucherand and E. Beaugnon, Magnetic susceptibility of high-curie-temperature alloys near their melting point, Phys. B: Condens. Matter **294-295**, 96 (2001).

[39] J. Wang, J. Li, R. Hu, H. Kou, and E. Beaugnon, Magnetic field enhanced phase precipitation in an undercooled Co–Sn alloy, Mater. Lett. **139**, 288 (2015).

[40] J. Wang, J. Li, R. Hu, H. Kou, and E. Beaugnon, Evidence for the structure transition in a liquid Co–Sn alloy by in-situ magnetization measurement, Mater. Lett. **145**, 261 (2015).

[41] X. Qiu, J. Li, J. Wang, T. Guo, H. Kou, and E. Beaugnon, Effect of liquid–liquid structure transition on the nucleation in undercooled Co–Sn eutectic alloy, Mater. Chem. Phys. **170**, 261 (2016).

[42] J. Wang, Y. He, J. Li, H. Kou, and E. Beaugnon, Strong magnetic field effect on the nucleation of a highly undercooled Co-Sn melt, Sci. Rep. **7**, 4958 (2017).

[43] J. Rodríguez-Carvajal, Recent advances in magnetic structure determination by neutron powder diffraction, Phys. B: Condens. Matter **192**, 55 (1993).

[44] A. Le Bail, Whole powder pattern decomposition methods and applications: A retrospection, Powder Diffr. **20**, 316 (2005).

[45] H. M. Rietveld, A profile refinement method for nuclear and magnetic structures, J. Appl. Crystallogr. **2**, 65 (1969).

[46] C. R. H. Bahl, Estimating the demagnetization factors for regular permanent magnet pieces, AIP Adv. **11**, 075028 (2021).

[47] Y. V. Khlebnikova, D. P. Rodionov, V. A. Sazonova, T. I. Tabatchikova, O. V. Antonova, Y. E. Turkhan, and V. A. Kazantsev, Study of the structure of cobalt single crystals during the $\beta \rightarrow \alpha$ transformation, Phys. Metals Metallogr. **103**, 609 (2007).

[48] A. Mikelson and Y. Karklin, Control of crystallization processes by means of magnetic fields, J. Cryst. Growth **52**, 524 (1981).

[50] R. Sewak, C. C. Dey, and D. Toprek, Temperature induced phase transformation in co, Sci. Rep. **12**, 10054 (2022).

[51] J. Burke and D. Turnbull, Recrystallization and grain growth, Prog. Met. Phys. **3**, 220 (1952).

[52] P. A. Beck, Annealing of cold worked metals, Adv. Phys. **3**, 245 (1954).

[53] D. A. Smith and C. M. F. Rae, Development in annealing and structure and mobility of grain boundaries in pure metals, Met. Sci. **13**, 101 (1979).

[54] C. Kittel, *Introduction to Solid State Physics*, 8th ed. (Wiley, New York, 2004).

[55] A. Taylor and R. W. Floyd, Precision measurements of lattice parameters of non-cubic crystals, Acta Crystallogr. **3**, 285 (1950).

[56] E. A. Owen and D. M. Jones, Effect of grain size on the crystal structure of cobalt, Proc. Phys. Soc. London, Sect. B **67**, 456 (1954).

[57] Y. Watanabe, The crystal structure of monoclinic γ-sulphur, Acta Crystallogr. Sect. B **30**, 1396 (1974).

[58] R. M. Moon, Distribution of magnetic moment in hexagonal cobalt, Phys. Rev. **136**, A195 (1964).

[59] R. A. Reck and D. L. Fry, Orbital and spin magnetization in fe-co, fe-ni, and ni-co, Phys. Rev. **184**, 492 (1969).

[60] T. Nishizawa and K. Ishida, The co (cobalt) system, Bull. Alloy Phase Diagrams **4**, 387 (1983).

[61] C. T. Chen, Y. U. Idzerda, H.-J. Lin, N. V. Smith, G. Meigs, E. Chaban, G. H. Ho, E. Pellegrin, and F. Sette, Experimental confirmation of the x-ray magnetic circular dichroism sum rules for iron and cobalt, Phys. Rev. Lett. **75**, 152 (1995).

[62] A. Jain, S. P. Ong, G. Hautier, W. Chen, W. D. Richards, S. Dacek, S. Cholia, D. Gunter, D. Skinner, G. Ceder, and K. A. Persson, Commentary: The materials project: A materials genome approach to accelerating materials innovation, APL Mater. **1**, 011002 (2013).

[63] M. K. Horton, J. H. Montoya, M. Liu, and K. A. Persson, High-throughput prediction of the ground-state collinear magnetic order of inorganic materials using density functional theory, npj Comput. Mater. **5**, 64 (2019).

[64] T. M. Project, Materials data on Co by materials project10.17188/1263614 (2020).

[65] F. Tran, G. Baudesson, J. Carrete, G. K. H. Madsen, P. Blaha, K. Schwarz, and D. J. Singh, Shortcomings of meta-gga functionals when describing magnetism, Phys. Rev. B **102**, 024407 (2020).

[66] L. A. Hall, Survey of electrical resistivity measurements on 16 pure metals in the temperature range 0 to 273 K, NBS Technical Note 365 (US Department of Commerce National Bureau of Standards, 1968).

[67] H. Nowotny and E. Gratz, Boltzmann equation and scattering mechanisms, in *Encyclopedia of Materials: Science and Technology*, edited by K. H. J. Buschow, R. W. Cahn, M. C. Flemings, B. Ilschner, E. J. Kramer, S. Mahajan, and P. Veyssière (Elsevier, Oxford, 2001), pp. 752–763.

[68] S. Flynn, C. L. Benyacko, M. Mihalik, J. Lee, F. Ma, M. E. Bates, S. Sinha, K. A. Abboud, M. W. Meisel, and J. J. Hamlin, Co-s eutectic in high magnetic fields - data sets - 2025 (2025).

[69] G. R. Stewart, Measurement of low-temperature specific heat, Rev. Sci. Instrum. **54**, 1 (1983).

[70] Z. P. Tener, S. Flynn, A. M. Donald, J. J. Hamlin, M. W. Meisel, M. V. Manuel, and M. S. Kesler, Thermocouples in resistive and induction furnaces operated in strong magnetic fields, IEEE Trans. Instrum. Meas. (2025), doi:10.1109/TIM.2025.3602597.

[71] See Supplemental Material at http://link.aps.org/supplemental/10.1103/9bb3-4pby for a technical manual about all aspects of the UF Physics $B \times T$ instrument.